新規ナノ $SnO_2/Pt_3Co/C$ 燃料電池触媒の調製と表面制御因子

岩　澤　康　裕*

*岩澤康裕　客員フェロー

Surface-regulated nano-$SnO_2/Pt_3Co/C$ cathode catalysts for PEFCs by a new electrochemical Sn deposition method

Yasuhiro IWASAWA*

We have found how to improve significantly the oxygen reduction reaction activity and durability with new nano-$SnO_2/Pt_3Co/C$ cathode catalysts in 0.1 M $HClO_4$, which were regulated by a new selective electrochemical Sn deposition method. The nano-$SnO_2/Pt_3Co/C$ catalysts with different Pt/Sn ratios were characterized to have a Pt_3Co core — Pt skeleton skin structure decorated with SnO_2 nano-islands at the compressive Pt surface with the defects and dislocations by means of STEM-EDS, XRD, XRF, XPS, *in-situ* XAFS, and electrochemical measurements. It was suggested that the high performances of the nano-$SnO_2/Pt_3Co/C$ electrocatalysts with Pt/Sn = 9/1 and 11/1 originate from two kinds of surface active sites (Site 1 and Site 2) produced by the SnO_2 nano-islandes at the Pt-enriched surface; Site 1 is the Pt skin surface and Site 2 is the periphery sites around nano SnO_2 at compressive Pt skeleton-skin surface. The Pt skin surface (Site 1) is electronically modified efficiently by both Co of the Pt_3Co core and surface nano-SnO_2 and the Site 2 possesses the unique property of the periphery sites of the SnO_2 nano-islands, which were estimated to be much more active than expected from the *d*-band center values. The white line peak intensity of the nano-$SnO_2/Pt_3Co/C$ revealed no hysteresis in the potential up-down operations between 0.4 V_{RHE} and 1.0 V_{RHE} unlike the cases of Pt/C and Pt_3Co/C, resulting in the high ORR performance and durability. The positive effect of nano SnO_2 was not observed on Pt nanoparticles. Further, when SnO_2 was supported on Pt_3Co/C by a conventional thermal supporting method, the supported SnO_2 did not show any significant promotion of the Pt_3Co/C electrocatalysis. The nano-$SnO_2/Pt_3Co/C$ fabricated by the selective electrochemical deposition method is regarded as a new class of cathode catalysts with two different active sites.

Introduction

Development of next-generation polymer electrolyte fuel cells (PEFCs) with high performance and durable cathode catalysts under harsh PEFC operating conditions is indispensable for widespread commercialization of PEFC vehicles even though TOYOTA MIRAI and HONDA CLARITY FUEL CELL were launched in market recently.[1–5] Various sorts of Pt-M alloys/C have been studied as one of the most promising candidates as cathode catalysts and many efforts have been devoted to fabrications of Pt-Co nanostructures with higher oxygen reduction reaction (ORR) activity and longer-term durability than Pt/C, while alloy nanoparticles are indicated to be unstable in acidic environments.[6–12] The Co additive effects on Pt/C have also been characterized by e.g. transmission electron microscopy,[13–15] *in-situ* time-resolved and spatially-resolved XAFS,[16–21] and theoretical calculations.[22–24] On the other hand, the Pt/C cathode catalysts have been modified by metal oxides such as SnO_x,[25–28] MoO_x,[29] CeO_x,[30] TiO_x,[31] and $Ti_{0.7}Mo_{0.3}O_2$[32] to change the redox behavior and improve ORR activity of Pt nanoparticles. The CeO_x additives were indicated to suppress Pt oxide formation and mitigate Pt particle aggregation though CeO_x with basic surface character dissolutes into acidic media. The $Ti_{0.7}Mo_{0.3}O_2$ mixed oxide was demonstrated to promote the ORR activity of Pt/C by electron transfer from the oxide to Pt.[32]

Recently, we found a new way to fabricate surface-regulated $SnO_2/Pt_3Co/C$ cathode catalysts with SnO_2 nano-islands on the Pt skeleton-skin surface with compressive strain and defects/dislocations on Pt_3Co nanoparticle cores, which were much more active than expected from the *d*-band center values.[33] The structural arrangement created two different reaction sites (Site 1 at the Pt skin surface and more active Site 2 at the nano-SnO_2 periphery) in a tunable mode with

2016年3月23日 受理
*豊田理化学研究所客員フェロー
電気通信大学燃料電池イノベーション研究センター
電気通信大学教授
東京大学名誉教授，理学博士
専門分野：触媒化学，表面科学，X線分光学

different Pt/Sn ratios, resulting in much more ORR activity and durability than Pt/C catalyst at rotating disk electrodes (RDE) in 0.1 M $HClO_4$. This remarkable promotion effect of nano SnO_2 on Pt_3Co/C was not observed with nano SnO_2 on Pt/C. SnO_2 supported on Pt_3Co/C by a conventional thermal non-selective Sn supporting method did not show any significant promotion effect on the Pt_3Co/C ORR performance. Here the fabrication, performance and characterization of the nano $SnO_2/Pt_3Co/C$ catalysts with different Pt/Sn ratios are summarized by showing several typical data.[33]

Preparation of $SnO_2/Pt_3Co/C$ catalysts[33]

A given amount (0.144 g, 0.086 g, or 0.062 g) of $SnCl_2$ was dissolved to 0.1 M $HClO_4$ aqueous solution (100 mL), to which 1 g of Pt_3Co/C was added and suspended under stirring. After stirring for 30 min, the potential of –0.45 V vs. Ag/AgCl was applied to the solution for 5 days. The best reduction potential for achieving the selective deposition and fast reduction of Sn species on Pt_3Co nanoparticles with Pt enriched surfaces predominantly and the Sn^0 deposition on the carbon can be neglected. After filtration of the solution, the obtained sample was washed with 50 mL of ultrapure water (Milli-Q water, Milli-Q Co.) 15 times, followed by drying at 313 K under vacuum for 2 days, and by subsequent gentle oxidation with O_2 at room temperature for 1 day to form SnO_2 nano-islands. SnO_2 is stable without significant dissolution to the acidic media.[34] A series of $SnO_2/Pt_3Co/C$ catalysts with Pt/Sn = 4/1, 9/1, 11/1 and 15/1 were fabricated similarly by the selective electrochemical deposition of Sn metal (Sn^0) on Pt_3Co/C (TEC36E52, Tanaka Kikinzoku Kogyo).

XRD patterns for the $SnO_2/Pt_3Co/C$ samples identified the Pt_3Co alloy phase with *Pm3m* space group similar to the Pt_3Co/C. The white line intensity and feature of the normalized XANES spectra at Sn K-edge for the $SnO_2/Pt_3Co/C$ samples (Pt/Sn = 4/1 and 9/1) coincided with those for SnO_2, and the XPS binding energies for Sn $3d_{3/2}$ and $3d_{5/2}$ levels (495.2 and 487.1 eV) for the $SnO_2/Pt_3Co/C$ samples were essentially similar to those for SnO_2 and no metallic Sn 3*d* XPS peaks were observed. These results evidence that the Sn atoms electrochemically deposited on the Pt_3Co nanoparticle surface were oxidized to SnO_2 under O_2 atmosphere at room temperature for 1 day.[33] The binding energies of the Pt $4f_{5/2}$ and $4f_{7/2}$ XPS peaks (74.7 and 71.6 eV, respectively) for the Pt_3Co/C shifted by 0.2 eV to the lower binding energies compared to the values 74.9 and 71.8 eV for Pt/C, respectively, demonstrating electron transfer from Co to Pt due to Pt 4*f*–Co 3*d* hybridization.[33]

A Pt/C catalyst with a similar Pt particle size to the Pt_3Co particle size of the Pt_3Co/C catalyst (TEC36E52, Tanaka Kikinzoku Kogyo) was also prepared for comparison. Commercial Pt/C (TEC10E50E, Tanaka Kikinzoku Kogyo) with 2.5–3.0 nm Pt nanoparticles was heated from room temperature to 823 K at a heating rate of 4.2 K min^{-1} and kept at 823 K for 2 h in a flow of N_2 at 5 mL min^{-1}.

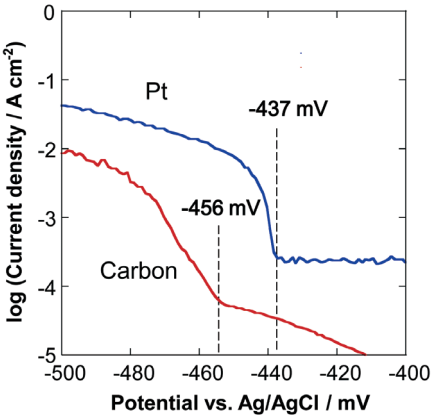

Figure 1. Tafel plots for Pt and carbon working electrodes at 60 s per 1 mV with Ag/AgCl reference electrode in 0.1 M $HClO_4$ solution involving 50 mM $SnCl_2$.[33]

Characterizations[33]

Field-emission transmission electron microscope (FE-TEM, JEM-2100F, JEOL) equipped with an energy dispersive spectrometer (EDS) was used for line scans and point spectra of the catalyst nanoparticles. The FE-TEM was operated at 200 kV in the scanning mode. The EDS line analysis revealed a Pt-enriched surface, which is partly covered by SnO_2 nano-islands. The Co signal in the EDS profile was negligible near the surface. XPS Co 2*p* signals in Figure S4 were not detected for all the $SnO_2/Pt_3Co/C$ samples (Pt/Sn = 11/1, 9/1 and 4/1) as well as the Pt_3CO/C sample, which also augments the fact of Pt surface-enriched nanoparticles. In the $SnO_2/Pt_3Co/C$ prepared by the selective electrochemical Sn deposition method, all SnO_2 species observed by TEM were located on the nanoparticles. In general, adhesion of transition metal oxides on carbon induces depression of the electrical conductivity of the carbon. Hence, the selective nano-SnO_2 decoration on the Pt surface-enriched nanoparticles provides a significant advantage as a cathode catalyst. The interatomic distances in the lattice contrast profiles in an HR-TEM image obtained by 0.2 nm electron-beam scanning were estimated to be 0.194 nm, 0.198 nm and 0.334 nm for $Pt_3Co(200)$, Pt(200) and $SnO_2(110)$ planes, respectively. The TEM images for the as-fabricated $SnO_2/Pt_3Co/C$ revealed the Pt surface-enriched Pt_3Co nanoparticles with two-three Pt surface layers,

similar to the case of a Pt_3Co/C sample. These results indicate that the SnO_2 nano-islands on the Pt skin in the as-fabricated $SnO_2/Pt_3Co/C$ sample did not break the geometric feature of the Pt shell-Pt_3Co core structure.[33]

Figure 2 (a) and (c) are the HR-TEM images of the Pt_3Co/C and $SnO_2/Pt_3Co/C$ (Pt/Sn = 9/1) after the aging, respectively, which show the atomic arrangements of typical (111) planes of Pt_3Co nanoparticles. The lattice contrast profiles of Figure 2 (b) along the red and blue arrows in (a) for a Pt_3Co/C particle revealed the regular Pt_3Co(220) interplane distance (0.195 nm) for the Pt_3Co core and the Pt(220) interplane distances (two sorts of distances 0.196 nm and 0.199 nm) for the three surface layers, indicating heterogeneous Pt arrangements at the surface after the aging treatment.[33]

The HR-TEM image for the $SnO_2/Pt_3Co/C$ with Pt/Sn = 9/1 after the aging in Figure 2 (c) exhibited that the Pt-enriched surface possessed many atomic defects and dislocations compared to the Pt_3Co/C surface as indicated typically by yellow arrows. The lattice contrast profiles in Figure 2 (d) along the red, blue, and green arrows near the defects and dislocations (a–e) in Figure 2 (c) showed the irregular intensities and intervals, which evidence a rough/skeleton surface morphology at the Pt surface layers. The atomic arrangements averaged with 10 surface atoms showed totally the 0.194–0.195 nm interplane distances, indicating the compressive strain at the Pt surface layers due to the effect of the underlying Pt_3Co core structure with the shorter lattice distance than that for pure Pt. The surface also involved the less compressive areas with the 0.198 nm interplane distance, indicating an inhomogeneous aspect of the Pt skeleton surface.[33]

Figure 2 (e) and (f) are a TEM image of the $SnO_2/Pt_3Co/C$ catalyst (Pt/Sn = 9/1) (same particle as (c)) and EDS line profiles for Pt (blue), Co (red) and Sn (green) along the light blue line of the TEM image, showing the Pt-enriched surface with SnO_2 nano-islands. The surface inhomogeneity may be partly due to heterogeneous distribution of SnO_2 nano-islands with approximately 0.4–1.3 nm dimension at the Pt surface as shown in the EDS profile of Figure 2 (f). The electrochemical Sn deposition on the Pt-skin surface of Pt_3Co nanoparticles at the potential of –0.45 V vs. Ag/AgCl induces surface Pt-Sn alloy formation as well as simple Sn adsorption, and the subsequent surface oxidation of the adsorbed Sn atoms at the surface and the alloyed Sn atoms in the surface layers to form SnO_2 nano-islands should make the surface layers to be rough. Further, the leaching of the remaining Sn^0 atoms and a part of Co^0 atoms in the Pt_3Co nanoparticles by the aging treatments in the voltage range between 0.05–1.2 V_{RHE}

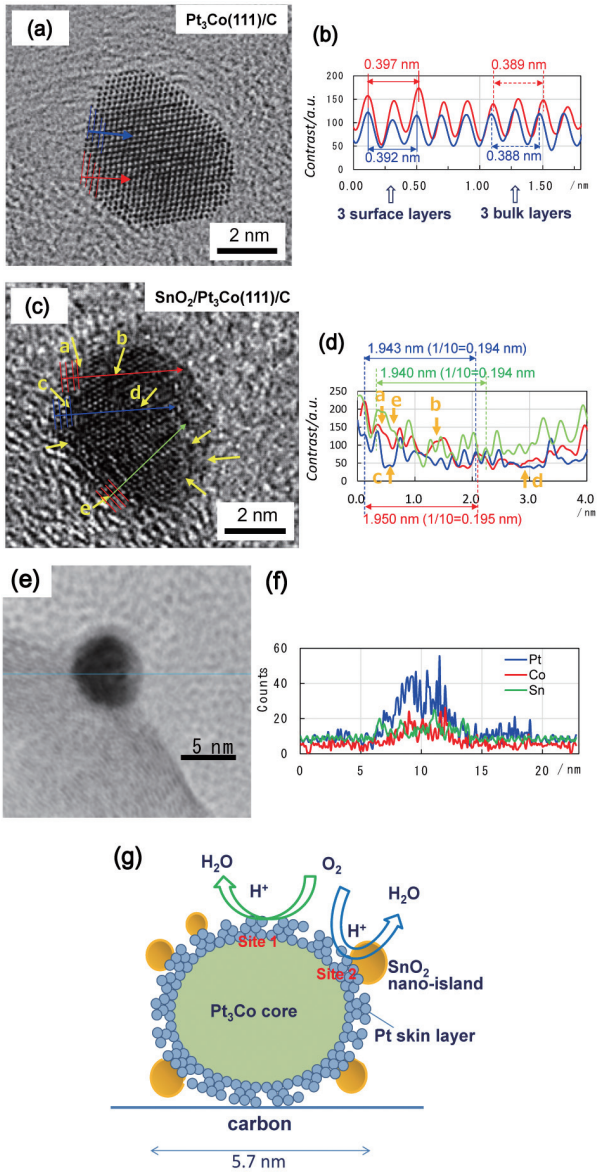

Figure 2. (a) Atomic arrangement of Pt_3Co(111) plane in a TEM image of the Pt_3Co/C after the aging. (b) Lattice contrast profiles for the interplane distances along the red and blue arrows of (a); The interplane distance around 0.195 nm in the Pt_3Co (220) direction and that around 0.199 nm in the Pt(220) direction. (c) Atomic arrangement of Pt_3Co(111) plane in a TEM image of the $SnO_2/Pt_3Co/C$ (Pt/Sn = 9/1) after the aging. Yellow arrows show typical defects and dislocations. (d) Lattice contrast profiles for the interplane distances along the red and blue arrows of (c), showing surface skeleton arrangements with defects and dislocations of Pt atoms; The 10-interplanes distance corresponds to 0.195 nm for the Pt_3Co(220) direction. (e) A TEM image of the $SnO_2/Pt_3Co/C$ catalyst (Pt/Sn = 9/1) (same particle as (c)) and (f) EDS line profiles for Pt (blue), Co (red) and Sn (green) along the light blue line of the TEM image, showing the Pt-enriched surface with SnO_2 nano-islands. (g) A model structure and proposed ORR sites (Site 1 and Site 2) for the nano-SnO_2-decorated Pt_3Co/C with Pt skeleton surface with compressive strain and defects/dislocations.[33]

at 50 mV s^{-1} in 0.1 M $HClO_4$ leaves many defects and dislocations behind their removal, and enhances the formation of a rough skeleton surface with increasing ECSAs as illustrated in Figure 2(g). The ECSAs of the $SnO_2/Pt_3Co/C$ (Pt/Sn = 4/1, 9/1, and 11/1) did not decrease until the ADT 10,000 load cycles, showing high stability.

The atomic arrangement in $Pt_3Co(111)$ plane and lattice contrast profiles for the $Pt_3Co(220)$ interplane distances in an HR-TEM image (a) and lattice contrast profiles (b) for $SnO_2/Pt_3Co/C$ (Pt/Sn = 9/1) after ADT 5,000 load cycles revealed the Pt-enriched skeleton-skin surface with defects and dislocations and with a compressive strain similar to the sample after aging.

Electrochemical and Material Properties of the Nano-$SnO_2/Pt_3Co/C$[33]

The electrochemical properties of the catalysts were measured at RDE in 0.1 M $HClO_4$ by using 10 μL of a mixture of absolute ethanol (1750 μL), ultra pure water (750 μL), 5% Nafion solution (25 μL) and catalyst powder (4.4 μg-Pt cm^{-2}) deposited on glassy carbon (GC) electrode (ϕ = 5 mm) and dried at room temperature in ambient air. The catalysts at the RDE were treated by 50 aging cycles between 0.05–1.2 V vs RHE (V_{RHE}) at 50 mV s^{-1} in N_2-saturated 0.1 M $HClO_4$ solution. Cyclic voltammetries (CV) were performed between 0.05–1.2 V_{RHE} at 50 mV s^{-1} and liner sweep voltammetries (LSV) were carried out from 0.05 to 1.0 V_{RHE} at 10 mV s^{-1}. Accelerated durability tests (ADT) were performed by rectangular load cycles (upto 10,000 cycles) between 0.6 and 1.0 V_{RHE} (6 s for each cycle). The electrochemical surface areas (ECSA) were estimated using the integration of hydrogen absorption and desorption areas in CV curves.

The electrochemical properties of the $SnO_2/Pt_3Co/C$ catalysts with different Pt/Sn ratios after the aging were measured at RDE in 0.1 M $HClO_4$. CV curves for $SnO_2/Pt_3Co/C$ (Pt/Sn = 9/1) and Pt_3Co/C after the aging (ADT 0 cycle) and ADT 1,000–5,000 cycles. The addition of a small amount of Sn to the Pt_3Co/C (Pt/Sn = 11/1) showed a slight increase in the ECSA, and the more Sn addition (Pt/Sn = 9/1) increased the

ECSA (electrochemical surface area) 2.0 times compared to that of the Pt_3Co/C though their particle sizes are similar. The ECSA decreased a little by the further Sn addition (Pt/Sn = 4/1) due to increasing physical block of the nano-SnO_2.

Oxygen reduction reaction (ORR) activities of the fabricated cathode catalysts were estimated by linear sweep voltammetry (LSV) at 0.9 V_{RHE} (Figure 3(a) and (b)), and mass activities (MAs) and surface specific activities (SAs)

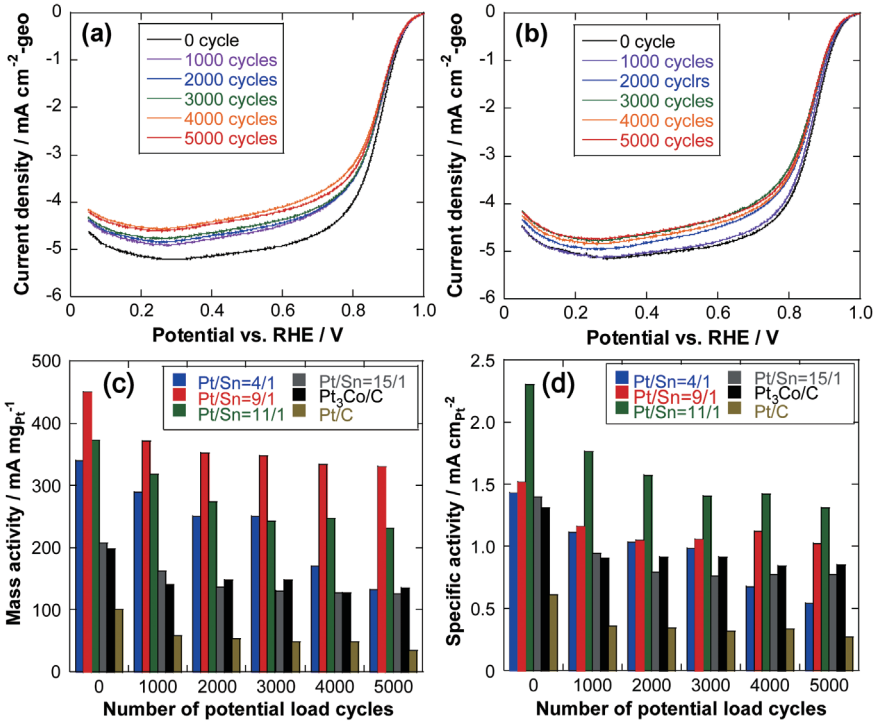

Figure 3. (a) and (b) Typical LSV curves at 1,600 rpm for the $SnO_2/Pt_3Co/C$ catalyst with Pt/Sn = 9/1 and Pt/Sn = 11/1, respectively after the ADT 0–5,000 cycles at RDE (4.4 μg-Pt cm^{-2}) in 0.1 M $HClO_4$. (c) and (d): Mass activities and surface specific activities, respectively, at 0.9 V_{RHE} for the $SnO_2/Pt_3Co/C$ with Pt/Sn = 4/1, 9/1, 11/1, and 15/1), Pt_3Co/C and Pt/C.[33] The ECSA, MA and SA values for 10,000 load cycles are shown in Ref.33 (supporting information).

for the $SnO_2/Pt_3Co/C$ (Pt/Sn = 4/1, 9/1, 11/1 and 15/1), Pt_3Co/C, and Pt/C catalysts were estimated by the Koutecky-Levich plots calculated from the LSV curves as shown in Figure 3 (c) and (d), respectively. The MA of the Pt_3Co/C was 2.2 times larger than that of the Pt/C, which is among the MA values in the literature.[8,11,13,15,19] It is to be noted that the MA of the Pt_3Co/C further 2.4 times increased by the SnO_2 addition (Pt/Sn = 9/1). Thus, the MA of the $SnO_2/Pt_3Co/C$ catalyst (Pt/Sn = 9/1) was 5.4 times larger than that of the Pt/C catalyst. This is contrasted to the fact that SnO_2 nano-islands in a SnO_2/Pt/C sample without Co similarly fabricated did not promote the Pt/C performance. The surface atomic arrangement of SnO_2/Pt/C (Pt/Sn = 5/1) did not show any compressive strain though there were defects and dislocations. The advantage of the $SnO_2/Pt_3Co/C$ (Pt/Sn = 9/1) also maintained after the 5,000 load cycles, where the MA of the $SnO_2/Pt_3Co/C$ was 7.8 times larger than that of the Pt/C, showing the high durability of the $SnO_2/Pt_3Co/C$. Figure 6 (c) reveals that there is an optimum SnO_2 amount for the ORR promotion and the durability improvement. The highest SA at 0.9 V_{RHE} among the $SnO_2/Pt_3Co/C$ catalysts after the aging was observed with the Pt/Sn = 11/1 catalyst as a result of the relatively smaller ECSA. The SA of the $SnO_2/Pt_3Co/C$ with Pt/Sn = 11/1 after the 5,000 load cycles was 5.0 times larger than that of the Pt/C. However, the SA of the Pt/Sn = 4/1 decreased almost linearly with the load cycles. Thus, the MA and SA of the $SnO_2/Pt_3Co/C$ catalysts are most promoted around Pt/Sn = 9-11/1.

The activities of the nano-$SnO_2/Pt_3Co/C$ catalysts with Pt/Sn = 9-11/1 were comparable to those of the top-level samples reported to date. The nano-$SnO_2/Pt_3Co/C$ also showed the much better durability than Pt/C. Thus, the catalyst fabrication method by the selective electrochemical Sn deposition may be promising because the method can be applied to any bimetal systems.

Key issues of high performance and durability of the Nano-$SnO_2/Pt_3Co/C$[33]

To examine the possibility that the promoting effect of the SnO_2 nano-islands may originate from adjustment of the *d*-band center of the catalysts we have measured CO stripping potentials. The CO stripping potentials at Pt and Pt-alloy nanoparticle surfaces correlate directly with Pt *d*-band center. The CO stripping potential peaks for Pt/C and Pt_3Co/C were observed at 800–900 mV as shown in Figure 4 (a). As for the $SnO_2/Pt_3Co/C$ with Pt/Sn = 15/1, 11/1, 9/1, and 4/1, the new peaks at the lower potentials in addition to the 800–900 mV peaks were also observed as discussed hereinafter. The surface sites for the 800–900 mV peaks are assigned as Site 1 at the Pt surface in Figure 2 (g). The SAs of the catalysts were plotted against the CO stripping peak potentials in Figure 4 (b), which changed as follows, Pt/C < Pt_3Co/C < $SnO_2/Pt_3Co/C$ (Pt/Sn = 15/1) < $SnO_2/Pt_3Co/C$ (Pt/Sn = 11/1) > $SnO_2/Pt_3Co/C$ (Pt/Sn = 9/1) > $SnO_2/Pt_3Co/C$ (Pt/Sn = 4/1), resulting in the volcano relationship between the CO stripping peak potentials (relative *d* band centers)and the SAs as shown in Figure 4 (b). The SAs of Pt-alloy catalysts have also been demonstrated to reveal a volcano relationship with their *d*-band center energies as shown in the green dotted line of Figure 4 (b), where the two values reported in the literature for each Pt/C (1), Pt_3Ni/C (2), Pt_3Co/C (3), Pt_3Fe/C (4), Pt_3V/C (5) and

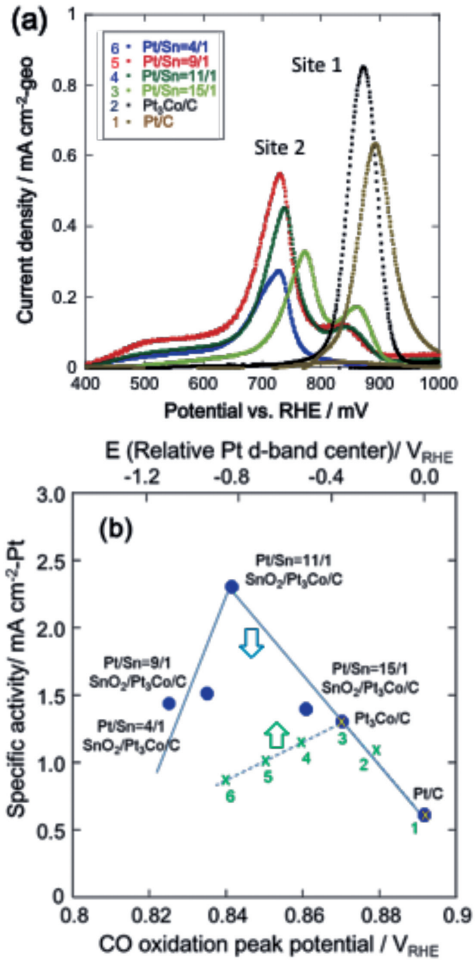

Figure 4. (a) CO stripping peak potentials for Pt/C (1), Pt_3Co/C (2), $SnO_2/Pt_3Co/C$ with Pt/Sn = 15/1 (3), 11/1 (4), 9/1 (5), and 4/1 (6). (b) Correlation between the specific activity (SA) and the CO stripping peak potentials for the $SnO_2/Pt_3Co/C$ (Pt/Sn = 4/1, 9/1, 11/1, and 15/1), Pt_3Co/C and Pt/C. The green dotted line: averaged from the data of two Refs. 20 and 34 for Pt/C(1), $Pt_3Ni/C(2)$, $Pt_3Co/C(3)$, $Pt_3Fe/C(4)$, Pt_3V/C (5) and $Pt_3Ti/C(6)$ was also shown by scaling of the relative *d*-band center, where the values of Pt/C and Pt_3Co/C (yellow x points) from Refs. 20 and 34 were normalized to the values in the present study.[33]

Pt_3Ti/C (6) were averaged and the values for the Pt_3Co/C and Pt/C were normalized to the CO stripping peak potentials measured in this study for comparison.[33] Thus, it is to be noted that the nano-SnO_2 in the $SnO_2/Pt_3Co/C$ with a compressive strain at the Pt skeleton surface layers electronically modified the 5*d* level to decrease the *d* band center, which leads to weaker oxygen adsorption and improvement of the ORR.

However, the same *d*-band center value did not show the same ORR activity (Figure 4 (b)), which indicates the existence of another factor for the ORR promotion in case of the $SnO_2/Pt_3Co/C$ catalysts in addition to the appropriate adjustment of *d*-band center at the Pt surface sites (Site 1). The additional CO stripping peaks at the much lower potentials (700–800 mV) appeared with the nano-SnO_2-decorated catalysts (Figure 4 (a)), which are regarded to be due to the event at new surface sites (Site 2). The redox change of SnO_2 cannot be responsible for the promotion due to preferable Sn^{4+} states in the range 0.4–1.0 V_{RHE} from the redox potential of Sn atoms. Thus, we propose that the periphery sites of the SnO_2 nano-islands with proton affinity at the Pt skeleton surface may provide the lower potential CO stripping sites and hence new ORR sites (Site 2 in Figure 2 (g)) for more weakly adsorbed O_2, facilitating the H^+-O_2 interaction.

To obtain the electronic and structural information on the nano-$SnO_2/Pt_3Co/C$ catalysts, we conducted *in-situ* XAFS measurements at RDE in 0.1 M $HClO_4$ by using a home-made *in-situ* XAFS cell. XAFS measurements at Pt L_{III}-edge and Sn K-edge for the $SnO_2/Pt_3Co/C$ catalysts were conducted by Si(111) and Si(311) double-crystal monochromators, respectively in a fluorescence mode using ion chambers (I_0: Ar 15%/ N_2 85% for Pt L_{III} edge and Ar 75%/ Kr 25% for Sn K-edge; I_f: Ar 70%/N_2 30% for Pt L_{III}-edge and Kr 100% for Sn K-edge) for incident and fluorescent X-rays, respectively at BL01B1and BL40XU stations (for powder samples), and *in situ* Pt L_{III}-edge, Co K-edge and Sn K-edge XAFS spectra at rotating disk electrodes (RDE) in 0.1 M $HClO_4$ were measured by using a 21 Ge-elements detector at BL36XU station in SPring-8. X-ray absorption near-edge structure (XANES) spectra were normalized by Athena software.[35] The XAFS spectra were treated with the data analysis program IFEFFIT (version 1.2.11c).[36] Theoretical phase and amplitude functions were calculated from FEFF 8.20.[37]

The white line peak intensity reflects the degree of the vacancy of Pt 5*d* orbitals near the Fermi level. In the potential gain processes from 0.4 V_{RHE} to 1.0 V_{RHE} the catalysts showed an increase of the white line intensity above 0.8 V_{RHE} (Figure 5), indicating a positive charge of the Pt surfaces due to Pt-O bonding.[38] In the potential down processes from 1.0 V_{RHE} to 0.4 V_{RHE} the white line responses for the Pt/C and Pt_3Co/C did not retrace those in the potential gain processes,

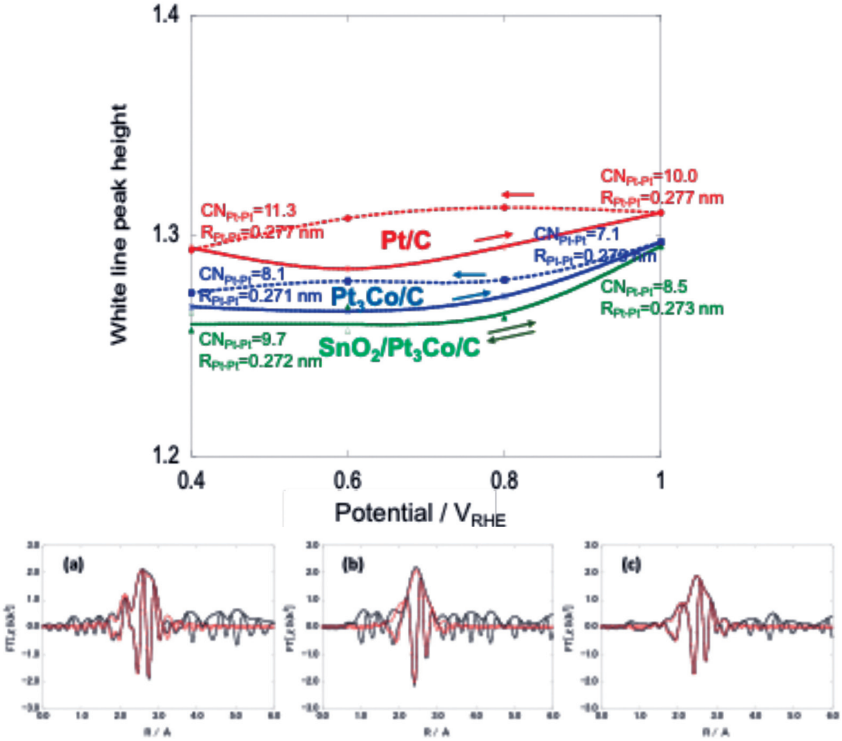

Figure 5. White line peak heights in the XANES spectra for Pt/C (red), Pt_3Co/C (blue) and $SnO_2/Pt_3Co/C$ with Pt/Sn = 11/1 (green) in the potential gain and down processes every 0.2 V between 0.4 V_{RHE} and 1.0 V_{RHE}. $CN_{Pt\text{-}Pt}$ and $R_{Pt\text{-}Pt}$: coordination numbers and bond distances for Pt-Pt at 0.4 V_{RHE} and 1.0 V_{RHE} (Table S1 and Figures S15–17.). (Bottom) EXAFS Fourier transforms and curve-fittings for Pt/C (a), Pt_3Co/C (b), and $SnO_2/Pt_3Co/C$ (Pt/Sn = 11/1) (c) at 0.4 V_{RHE}.[33]

showing a definite hysteresis. It is notable that the nano-SnO_2/Pt_3Co/C exhibited no hysteresis in the potential operations between 0.4 V_{RHE} and 1.0 V_{RHE}. Oxygen species adsorbed on the $SnO_2/Pt_3Co/C$ surface at 1.0 V_{RHE} are readily reduced below 1.0 V_{RHE}, resulting in the higher ORR performance. The *in-situ* Co K-edge XANES spectra analysis for the SnO_2/Pt_3Co/C (Pt/Sn = 11/1) in the potential operations revealed no change in the Co states of the Pt_3Co core. *In-situ* Sn K-edge XANES spectra with good quality in the potential operations could not be tracked, but our previous study for the MEA Pt-Sn(oxidized)/C samples evidenced no change in the Sn states in 200 I-V load cycles, indicating a high stability under the PEFC operating conditions. The *ex-situ* XANES spectra and EXAFS oscillations and Fourier transforms at Pt L_{III}-edge, Co K-edge and Sn K-edge after aging and ADT 5,000 cycles did not change, respectively, which suggests that the electronic states and local structures of Pt, Co and Sn atoms in the $SnO_2/Pt_3Co/C$ samples remained unchanged after the ADT 5,000 load cycles. These data also reveal the high durability of the $SnO_2/Pt_3Co/C$ samples under the PEFC operating conditions.

The compressive strain at the Pt surface layers was also suggested by the shorter Pt-Pt bond distances (0.271–0.272 nm) for the Pt_3Co/C and $SnO_2/Pt_3Co/C$ catalysts compared to 0.277 nm for the Pt/C catalyst with the similar Pt nanoparticle size (Figure 5 (a), (b) and (c)), which were decided by the *in-situ* EXAFS curve-fitting analysis in Figure 5 (a)–(c). The oxygen adsorption at 1.0 V_{RHE} caused the decrease in the coordination number of Pt-Pt bonds probably due to the distorted rearrangement of Pt atoms at the topmost layer by the Pt-O bonding. The ORR promotion by the SnO_2 nano-islands decoration is not referred to the down-shift of the *d*-band center for the Pt skeleton layers (Site 1) because the too much reduction of the *d*-band center level decreases the SAs for Pt_3V/C and Pt_3Ti/C (Figure 4 (b)), but rather to the new reactive periphery sites (Site 2) of the SnO_2 nano-islands at the Pt skeleton surface (Figure 2 (g)). The ECSA of the periphery sites is not clear at moment because the CO adsorption cannot simply be compared to the hydrogen adsorption in the case of the rough skeleton surface, but if the periphery area (Site 2) is provisionally one third or half of the ECSA, the SA of Site 2 in the $SnO_2/Pt_3Co/C$ with Pt/Sn = 11/1 is estimated to be 7.8 times or 5.2 times, respectively, larger than the SA of Site 1 expected from the *d*-band center value.

Conclusions

In conclusion the significant improvements for the ORR activity and durability were achieved with the new nano-SnO_2/Pt_3Co/C catalysts, which were regulated by a new selective electrochemical Sn deposition method and subsequent chemical treatments. The nano-$SnO_2/Pt_3Co/C$ catalysts with Pt/Sn = 9/1 and 11/1 were among the samples with the highest level performances reported to date. The nano-$SnO_2/Pt_3Co/C$ catalysts after the aging treatments possessed a Pt_3Co core/Pt skeleton-skin structure decorated with SnO_2 nano-islands at the surface. Their high performances originated from the unique reactive periphery sites of the SnO_2 nano-islands at the compressive Pt skeleton surface (Pt-Pt distance: 0.272 nm) with the defects and dislocations in addition to the compressive Pt skin surface. The ORR activity and durability of Pt_3Co/C were tuned by changing the amount of surface SnO_2 nano-islands. The white line peak intensity of the nano-$SnO_2/Pt_3Co/C$ revealed no hysteresis in the potential up-down operations between 0.4 V_{RHE} and 1.0 V_{RHE} unlike the cases of Pt/C and Pt_3Co/C, indicating the weaker oxygen adsorption and higher ORR activity compared to the Pt/C and Pt_3Co/C. The present results provide a new insight into development of a new class of next-generation PEFC cathode catalysts with two different active sites.

Acknowledgments

The XAFS measurements were performed with the approval of SPring-8 subject number 2011B1597, 2012A1004, 2012B1023, 2012B1025, 2013B7802, 2014A7800, 2014A7805, 2014B7800, 2015A7803, and 2015B7800. Y.I thanks Toyota Physical and Chemical Research Institute for supporting researches of next-generation fuel cell and green sustainable catalysis. The part of this work was supported by the New Energy and Industrial Technology Development Organization (NEDO) of Japan.

References

(1) Debe, M. K. *Nature* (2012) **486**, 43-51.
(2) Rabis, A.; Rodriguez, P.; Schmidt, T. J. *ACS Catal.* (2012) **2**, 864-890.
(3) Wu, G.; More, K. L.; Johnston, C. M.; Zelenay, P. *Science* (2011) **332**, 443-447.
(4) Strasser, P.; Koh, S.; Anniyev, T.; Greeley, J.; More, K.; Yu, C.; Liu, Z.; Kaya, S.; Nordlund, D.; Ogasawara, H.; Toney, M. F.; Nilsson, A. *Nat. Chem.* (2010) **2**, 454-460.
(5) Wu, J.; Yang, H. *Acc. Chem. Res.* (2013) **46**, 1848-1857.
(6) Xin, H. L.; Mundy, J. A.; Liu, Z.; Cabezas, R.; Hovden, R.; Kourkoutis, L. F.; Zhang, J.; Subramanian, N. P.; Makharia, R.; Wagner, F. T.; Muller, D. A. *Nano Lett.* (2012) **12**, 490-497.
(7) Koh, S.; Strasser, P. *J. Am. Chem. Soc.* (2007) **129**, 12624-12625.

(8) Loukrakpam, R.; Luo, J.; He, T.; Chen, Y. S.; Xu, Z.; Njoki, P. N.; Wanjala, B. N.; Fang, B.; Mott, D.; Yin, J.; Klar, J.; Powell, B.; Zhong, C. *J. Phys. Chem. C* (2011) **115**, 1682-1694.

(9) Mani P.; Srivastava, R.; Strasser, P. *J. Power Sorces* (2011) **196**, 666-674.

(10) Wang, C.; Chi, M.; Li, D.; Strmcnik, D.; van der Vliet, D.; Wang, G.; Komanicky, V.; Chang, K.; Paulikas, A. P.; Tripkovic, D.; Pearson, J.; More, K. L.; Markovic, N. M.; Stamenkovic, V. R. *J. Am. Chem. Soc.* (2011) **133**, 14396-14403.

(11) Stamenkovic, V. R.; Mun, B. S.; Arenz, M.; Mayrhofer, K. J. J.; Lucas, C. A.; Wang, G.; Ross, P. N.; Markovic, N. M. *Nat. Mater.* (2007) **6**, 241-247.

(12) Carlton, C. E.; Chen, S.; Ferreira, P. J.; Allard, L. F.; Shao-Horn, Y. *J. Phys. Chem. Lett.* (2012) **3**, 161-166.

(13) Wang, D.; Xin, H. L.; Hovden, R.; Wang, H.; Yu, Y.; Muller, D. A.; DiSalvo, F. J.; Abruña, H. D. *Nature Mater.* (2012) **12**, 81-87.

(14) Yu, Y.; Xin, H. L.; Hovden, R.; Wang, D.; Rus, E. D.; Mundy, J. A.; Muller, D. A.; Abruna, H. *Nano Lett.* (2012) **12**, 4417-4423.

(15) Heggen, M.; Oezaslan, M.; Houben, L.; Strasser, P. *J. Phys. Chem. C* (2012) **116**, 19073-19083.

(16) Tada, M.; Murata, S.; Asaoka, T.; Hiroshima, K.; Okumura, K.; Tanida, H.; Uruga, T.; Nakanishi, H.; Matsumoto, S.; Inada, Y.; Nomura, M.; Iwasawa, Y. *Angew. Chem. Int. Ed.* (2007) **46,** 4310-4315.

(17) Ishiguro, N.; Saida, T.; Uruga, T.; Nagamatsu, S.; Sekizawa, O.; Nitta, K.; Yamamoto, T.; Ohkoshi, S.; Iwasawa, Y.; Yokoyama, T.; Tada, M. *ACS Catal.* (2012) **2**, 1319-1330.

(18) Ishiguro, N.; Kityakarn, S.; Sekizawa, O.; Uruga, T.; Sasabe, T.; Nagasawa, K.; Yokoyama, T.; Tada, M. *J. Phys. Chem. C* (2014) **118**, 15874-15883.

(19) Saida, T.; Sekizawa, O.; Ishiguro, N.; Hoshino, M.; Uesugi, K.; Uruga, T.; Ohkoshi, S.; Yokoyama, T.; Tada, M. *Angew. Chem. Int. Ed.* (2012) **51**, 10311-10314.

(20) Takao, S.; Sekizawa. O.; Nagamatsu, S.; Kaneko, T.; Yamamoto, T.; Samjeské, G.; Higashi, K.; Nagasawa, K.; Tsuji, T.; Suzuki, M.; Kawamura, N.; Mizumaki, M.; Uruga, T.; Iwasawa, Y. *Angew. Chem. Int. Ed.* (2014) **53**, 14110-14114.

(21) Takao, S.; Sekizawa, O.; Samjeské, G.; Nagamatsu, S.; Kaneko, T.; Yamamoto, T.; Higashi, K.; Nagasawa, K.; Uruga, T.; Iwasawa, Y. *J. Phys. Chem. Lett.* (2015) **6**, 2121-2126.

(22) Stamenkovic, V. R.; Mun, B. S.; Mayrhofer, K. J. J.; Ross, P. N.; Markovic, N. M.; Rossmeisl, J.; Greeley, J.; Norskov, J. K. *Angew. Chem. Int. Ed.* (2006) **45**, 2897-2901.

(23) Matanovic, I.; Garzon, F. H.; Henson, N. J. *J. Phys. Chem. C* (2011) **115**, 10640-10650.

(24) Friebel, D.; Viswanathan, V.; Miller, D. J.; Anniyev, T.; Ogasawara, H.; Larsen, A. H.; O'Grady, C. P.; Nørskov, J. K.; Nilsson, A. *J. Am. Chem. Soc.* (2012) **134**, 9664-9671.

(25) Samjeské, G.; Nagamatsu, S.; Takao, S.; Nagasawa, K.; Imaizumi, Y.; Sekizawa, O.; Yamamoto, T.; Uemura, Y.; Uruga, T.; Iwasawa, Y. *Phys. Chem. Chem. Phys.* (2013) **15**, 17208-17218.

(26) Samjeské, G.; Nagamatsu, S.; Nagasawa, K.; Imaizumi, Y.; Takao, S.; Sekizawa, O.; Yamamoto, T.; Uruga, T.; Iwasawa, Y. *ECS Transactions* (2012) **50**, 1651-1657.

(27) Uemura, Y.; Inada, Y.; Bando, K. K.; Sasaki, T.; Kamiuchi, N.; Eguchi, K.; Yagishita, A.; Nomura, M.; Tada, M.; Iwasawa, Y. *J. Phys. Chem. C* (2011) **115**, 5823-5833.

(28) Uemura, Y.; Inada, Y.; Bando, K. K.; Sasaki, T.; Kamiuchi, N.; Eguchi, K.; Yagishita, A.; Nomura, M.; Tada, M.; Iwasawa, Y. *Phys. Chem. Chem. Phys.* (2011) **13**, 15833-15844.

(29) Ioroi, T.; Fujiwara, N.; Siroma, Z.; Yasuda, K.; Miyazaki, Y. *Electrochem. Commun.* (2002) **4**, 442-446.

(30) Masuda, T.; Fukumitsu, H.; Fugane, K.; Togasaki, H.; Matsumura, D.; Tamura, K.; Nishihata, Y.; Yoshikawa, H.; Kobayashi, K.; Mori, T.; Uosaki, K. *J. Phys. Chem. C* (2012) **116**, 10098-10102.

(31) Selvaganesh, S. V.; Selvarani, G.; Sridhar, P.; Pitchumani, S.; Shukla, A. K. *J. Electrochem. Soc.* (2010) **157**, B1000-B1007.

(32) Ho, V. T. T.; Pan, C. J.; Rick, J.; Su, W. N.; Hwang, B. J. *J. Am. Chem. Soc.* (2011) **133**, 11716-11724.

(33) Nagasawa, K.; Takao, S.; Nagamatsu, S.; Samjeské, G.; Sekizawa, O.; Kaneko, T.; Higashi, K.; Yamamoto, T.; Uruga, T.; Iwasawa, Y. *J. Am. Chem. Soc.* (2015) **137**, 12856-12864.

(34) Sasaki, K.; Takasaki, F.; Noda, Z.; Hyashi, S.; Shirotori, Y.; Ito, K. *ECS Trans.* (2010) **33**, 473-482.

(35) Newville, M.; Ravel, B.; Haskel, D.; Rehr, J. J.; Stern, E. A.; Yacoby, Y. *Physica B* (1995) **154**, 208-209.

(36) Ravel, B.; Newville, M. *J. Synchrotoron Rad.* (2005) **12**, 537-541.

(37) Ankudinov, A. L.; Ravel, B.; Rehr, J. J.; Conradson, S. D. *Phys. Rev. B* (1998) **58**, 7565.

(38) Nagamatsu, S.; Arai, T.; Yamamoto, M.; Ohkura, T.; Oyanagi, H.; Ishizaka T.; Kawanami, H.; Uruga, T.; Tada, M.; Iwasawa, Y. *J. Phys. Chem. C* (2013) **117**, 13094-13107.